ORIGINAL PAPER

Thermo-Mechanical Properties of Granite at Elevated Temperatures and Numerical Simulation of Thermal Cracking

Fei Wang[1] · Heinz Konietzky[1]

Abstract

A comprehensive data compilation, in respect to thermo-mechanical parameters, of granite exposed to temperatures up to about 1000 °C is presented. Most material parameters experience a significant change with increasing temperature connected with thermal-induced cracking. Some of them (tensile strength, Young's modulus, cohesive strength, thermal conductivity) show a continuous change, while the α–β transition of quartz leads to an abrupt jump in some other parameters (Poisson's ratio, thermal expansion coefficient, specific heat). Based on a compilation of these parameters, temperature-dependent relations have been deduced. These relations are combined with constitutive models based on the classical Mohr–Coulomb model with strain softening and tension cutoff. The obtained new constitutive law is validated by uniaxial compression tests on granite samples exposed to high temperatures up to 800 °C. The proposed numerical model is able to duplicate the thermal-induced cracking, which results in reduced peak strength, pronounced softening, and transition from brittle to ductile behaviour. Comparison with lab tests in respect to thermal-induced fracture pattern and stress–strain relations shows remarkable agreement. Simulations—supported also by lab tests—show, that up to about 200 °C no macroscopic damage occurs in the heated granite before loading; however, significant macroscopic damage occurs beyond 600 °C, which leads to reduced strength after cooling.

Abbreviations

C_v, C_v/C_{v0}	Specific heat and corresponding normalized value
E, E/E_0	Young's modulus and corresponding normalized value
E_c	Young's modulus calculated from peak axial stress and strain
E_{input}	Back-calculated Young's modulus
E_s	Young's modulus deduced from linear part of stress–strain curve
K	Bulk modulus
L, ΔL	Length of the sample and length increment
P_0, P_i	Property of the sample and the element i
T, T_0, T_{max}	Temperature, room temperature, and maximum temperature
$T_{\alpha-\beta}$	Temperature of α–β quartz transition
ΔT	Temperature increment
∇T	Temperature gradient
a, b	Coefficients of the linear equation
c, c/c_0	Cohesion and corresponding normalized value
$f_{Cv/Cv0}$	Fitting equation of normalized specific heat
$f_{c/c0}$	Fitting equation of normalized cohesion
$f_{E/E0}$	Fitting equation of normalized Young's modulus
$f_{k/k0}$	Fitting equation of normalized thermal conductivity
$f_{\alpha t/\alpha t0}$	Fitting equation of normalized linear thermal expansion coefficient
$f_{\nu/\nu0}$	Fitting equation of normalized Poisson's ratio
$f_{\sigma t/\sigma t0}$	Fitting equation of normalized tensile strength
$f_{\varphi/\varphi0}$	Fitting equation of normalized friction angle
k, k/k_0	Thermal conductivity and corresponding normalized value
m	Shape parameter of Weibull distribution
q_i	Heat flux vector
q_v	Volumetric heat-source intensity
t	Time

✉ Fei Wang
finn.wang@foxmail.com

1 Geotechnical Institute, TU Bergakademie Freiberg,
Gustav-Zeuner-Str. 1, 09596 Freiberg, Germany

x_0	Scale parameter of Weibull distribution
x_i	Weibull random variable for element i
α_t, α_t/α_{t0}	Linear thermal expansion coefficient and corresponding normalized value
β_t, β_t/β_{t0}	Volumetric thermal expansion coefficient and corresponding normalized value
δ_{ij}	Kronecker delta
δ_σ, δ_ε	Relative error of stress and strain
σ_t, σ_t/σ_{t0}	Tensile strength and corresponding normalized value
ε^e, ε^p	Elastic strain and plastic strain
ε^{pt}, ε^{ps}	Plastic tension strain and plastic shear strain
ε_v	Volumetric strain
ν, ν/ν_0	Poisson's ratio and corresponding normalized value
ρ	Density
σ_1, σ_3	Maximum and minimum principal stress
σ_c, ε_{1c}	Peak axial stress and axial strain obtained from lab test
σ_{cs}, ε_{cs}	Peak axial stress and axial strain obtained from simulation
$\Delta\sigma_{ij}$, $\Delta\varepsilon_{ij}$	Thermal stress and strain changes
φ, φ/φ_0	Friction angle and corresponding normalized value
ψ	Dilation angle (please note, that positive stress values mean tensile stress and negative values indicate compressive stress)

1 Introduction

High temperatures have an obvious impact on physical and mechanical properties of rocks, and these changes are complex and different for different types of rock (e.g., Brotóns et al. 2013; Gautam et al. 2016). Granite is one of the most common and interesting rocks. For instance, it is considered as the host rock for nuclear waste disposals (e.g., Heuze 1981), target formation for deep geothermal energy projects (e.g., Kumari et al. 2017a, b), and used as construction material including historical buildings, monuments and sculptures (e.g., Freire-Lista et al. 2016). Many researchers have conducted lab tests to investigate the physical properties and the mechanical behaviour of granites at high temperatures. Heuze (1983) provided an extensive literature review about high-temperature mechanical and transport properties of granitic rocks. David et al. (1999) presented data sets on the influence of stress-induced and thermal cracking on physical properties and microstructure of La Peyratte granite. Documented data show that thermal loading contributes to the interplay between the evolution of rock microstructures and variations of physical properties in granites. Dwivedi et al. (2008) studied various thermo-mechanical properties of Indian granite at high temperatures in the range of

30–160 °C. They also carried out a literature survey to collect data on the properties of different granites at high temperatures. Both lab test results and literature review show a temperature-dependent characteristic of granite properties.

When being exposed to heat flux, usually the main mineral composition of granite does not change with increasing temperatures (Saiang and Miskovsky 2012; Heap et al. 2013; Chen et al. 2017; Yang et al. 2017). However, the quartz within the granite undergoes a reversible change in crystal structure (the α/β phase transition) at about 573 °C. This leads to pronounced microcracking at the α/β phase transition temperature (Glover et al. 1995). Granites can be damaged by thermal cracking which is caused by the accumulation of internal stresses. Many researchers (e.g., Yong and Wang 1980; Heap et al. 2013) have found that thermal stresses are mainly controlled by (a) the constituents of the rocks (minerals and pore fillings have different thermal expansion characteristics), (b) thermal expansion anisotropy within individual minerals and, (c) thermal gradients.

Compared to the numerous lab tests of heated granite documented, numerical simulations of brittle rocks at fire or high temperatures (e.g., above 500 °C) are quite limited. Jiao et al. (2015) proposed a 2D discontinuum model for simulating thermal cracking of brittle rocks within the framework of the discontinuous deformation analysis (DDA) method, but the material deformation rate was assumed to be zero in the proposed model, i.e., the influence of material deformation on temperature cannot be considered. Shao et al. (2015) built a 2D finite element (FE) model for compression tests carried out on granite specimens at elevated temperatures. One of the drawbacks of this model is that uniform temperature across the entire granite is assumed. Therefore, thermal cracking cannot be simulated in a correct manner. Zhao (2016) elucidated the mechanisms responsible for temperature-dependent mechanical properties of granite using a particle-based approach, indicating that the strength reduction mainly results from the increasing thermal stresses and the generation of tensile microcracks. The boundary temperature was limited to 400 °C, because the model could not simulate some significant changes induced by the α–β quartz phase transition, and only monotonous changes in the mechanical behaviour were obtained because no temperature-dependent parameters were assigned in this model. Xu et al. (2017) proposed a two-dimensional thermo-mechanical model to describe the time-dependent brittle deformation (brittle creep) of granite under different constant temperatures and confining pressures. All parameters used in the model are constant and the maximum temperature was set to only 90 °C.

Previous simulations have usually applied some loading, constant properties and low or fixed temperatures. However, for some cases like buildings or sculptures exposed to fire, unconfined boundary conditions with different heating rates,

extremely high temperatures (e.g., 800 °C) and significant changes in properties are realistic. A comprehensive model for this issue is still missing.

Continuum-based methods are quite attractive, because they can reproduce different failure phenomena, from brittle to ductile including softening by averaging the effect of crack evolution and coalescence (Tan 2013). Therefore, in this study, the finite difference (FD) continuum code FLAC[3D] (Itasca 2018) is used with the aim to develop a new numerical scheme to simulate the thermal-induced damage of granite at high temperatures. The research strategy underlying the work in this study is illustrated in Fig. 1.

2 Thermo-Mechanical Properties of Granite

A literature review shows that most mechanical and thermal properties at high temperatures change dramatically compared to room temperature. Also, other strength properties like fracture toughness are influenced by thermal-induced cracking (Nasseri et al. 2007, 2009; David et al. 2012; Griffiths et al. 2017). The experimental data of granites used in this study are compiled based on a literature study. Since different granites have different property values, normalized values are used to detect tendencies without considering the influence of the individual granite type. Normalized property values P_t/P_{t0} relate the property values at elevated temperature (P_t) to the value at room temperature (P_{t0}). They are shown as functions of temperature.

2.1 Temperature-Dependent Mechanical Properties

2.1.1 Tensile Strength

Bauer and Johnson (1979) found that tensile strengths of Westerly and Charcoal granites do not exhibit a significant decrease until $T_{max} > 150$–200 °C. They also noticed that the variation of tensile strength with increasing temperatures has the greatest rate of change at $T_{\alpha-\beta}$ (α–β quartz transition) at about 573 °C. Generally, the tensile strength of granites decreases with increasing temperature from 25 to 1050 °C (e.g. Török and Török 2015) (Fig. 2). The normalized trend curve related to room temperature obtained by fitting is given by Eq. (1):

$$f_{\sigma_t/\sigma_{t0}} = \begin{cases} 0.9912(1 - 4.10T/2483.30)^{(1/4.10)}, & 0\ °C \le T \le 600\ °C \\ 2.610e^{-0.0036T}, & 600\ °C < T \le 1050\ °C. \end{cases}$$
(1)

2.1.2 Young's Modulus

Young's modulus decreases with increasing temperatures (Fig. 3). Some granites like Remiremont (Dwivedi et al. 2008) exhibit a slight increase within a certain temperature range (e.g., 25–200 °C), while some granites like Salisbury (Dwivedi et al. 2008) show a clear decrease at elevated temperatures. But for all granites, Young's modulus will drop significantly to a much lower value after a critical temperature (about 600 °C). The normalized trend curve is given by Eq. (2):

$$f_{E/E_0} = \begin{cases} 1.2665/(1 + e^{-1.430+0.0034T}), & 0\ °C < T \le 600\ °C \\ 1/(-109.953 + 17.542\ln(T)), & 600\ °C < T \le 1250\ °C. \end{cases}$$
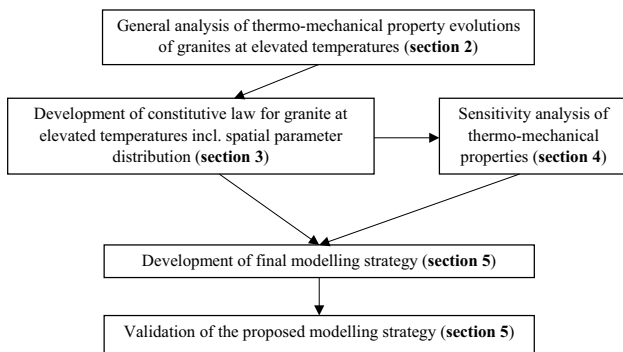(2)

Fig. 1 Research strategy and structure of the study

Fig. 2 Normalized tensile strength of granites vs. temperature
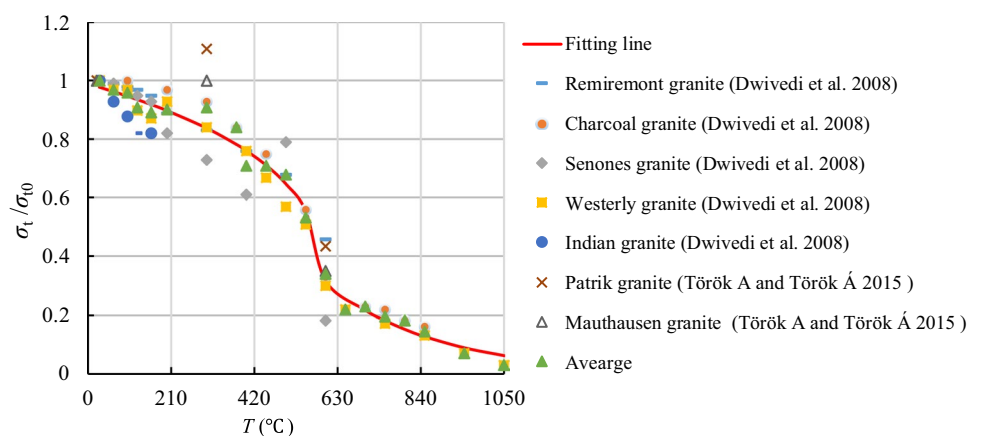
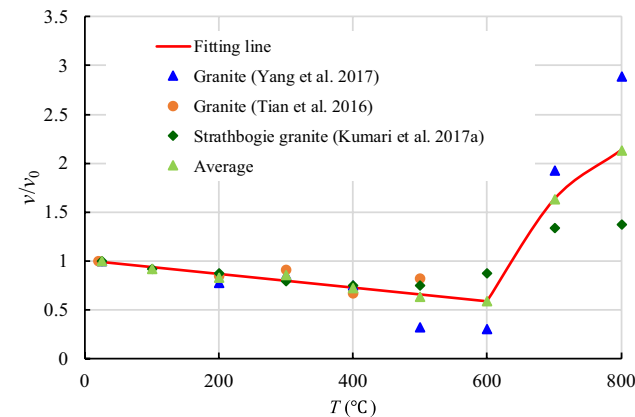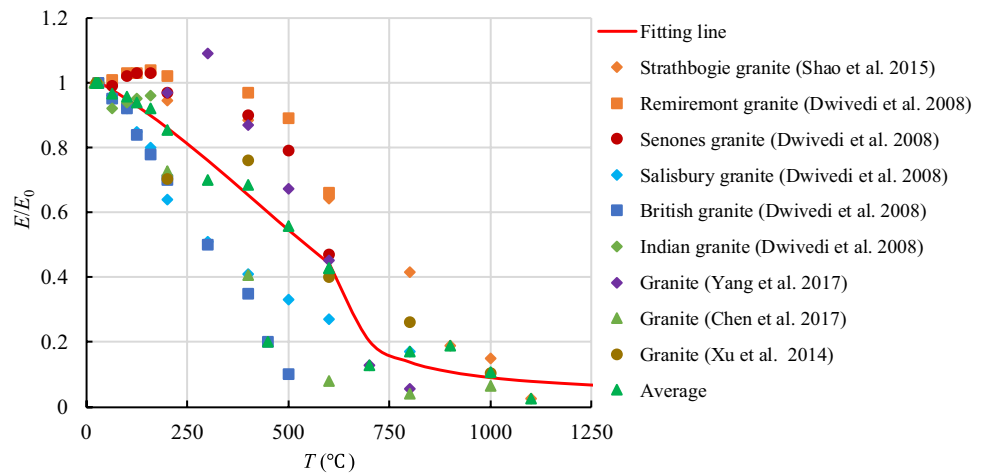**Fig. 3** Normalized Young's modulus of granites vs. temperature

Fig. 4 Normalized Poisson's ratio of granites vs. temperature

2.1.3 Poisson's Ratio

Poisson's ratio decreases gradually with increasing temperature between 25 and 600 °C (Fig. 4). However, the value increases strongly beyond a critical temperature (about 600 °C). But, this trend is not yet profound due to limited available experimental data beyond 600 °C and might be different for different types of granites. Equation (3) gives the normalized trend curve:

$$f_{\nu/\nu_0} = \begin{cases} -7 \times 10^{-4} T + 1.0052, & 0\ ^{\circ}\text{C} \leq T \leq 600\ ^{\circ}\text{C} \\ 2.240/(1 + e^{13.11 - 0.020T}), & 600\ ^{\circ}\text{C} < T \leq 800\ ^{\circ}\text{C} \end{cases}.$$

(3)

2.1.4 Cohesive Strength and Friction Angle

Since shear parameters in terms of cohesion and friction angle at high temperatures are quite rare in literature, data obtained from triaxial experiments were back analysed. The classical Mohr–Coulomb criterion can be given in the principal stress space as follows (Vásárhelyi 2009; Panji et al. 2016):

$$\sigma_1 = \frac{1 + \sin\varphi}{1 - \sin\varphi}\sigma_3 + \frac{2c\cos\varphi}{1 - \sin\varphi}.$$

(4)

Based on the equation above and the data obtained from the triaxial tests, a linear equation $\sigma_1 = a + b\sigma_3$ can be obtained by the least square method. Cohesion c and internal friction angle φ can be calculated according to the constants a and b (Tian et al. 2016):

$$\varphi = \arcsin\left(\frac{b-1}{b+1}\right)$$

(5)

$$c = \frac{a(1 - \sin\varphi)}{2\cos\varphi}.$$

(6)

Figure 5 shows that cohesion will generally decrease with increasing temperatures. The corresponding normalized trend curve is given by Eq. (7). However, friction angles of different granites show a distinct different pattern (Fig. 6), which means that the relationship between friction angle and temperature is hard to predict and may differ from granite to granite. The values for Westerly granite 1 (Dwivedi et al. 2008) are doubtful because we did not find the original data of the corresponding temperatures listed by Dwivedi in Bauer and Johnson's (1979) publication. We obtained different friction angles for Westerly granite (Bauer and Johnson 1979) by our back analysis of the triaxial data. The data for Westerly granite 2 (Dwivedi et al. 2008) are obtained at high confining pressure and the Hoek–Brown criterion (Hoek and Brown 1997) may be more appropriate than the Mohr–Coulomb model. We should also notice that only Westerly granite 1 and 2 show an obvious reduction in friction angle, for other granites, friction is rather constant or becomes even slightly higher at elevated temperatures (e.g. Friedman et al. 1979; Xu et al. 2014). Although we obtained a trend curve as given by Eq. (8), compared with cohesion, the temperature dependency of friction angle is less significant and to some extent questionable:

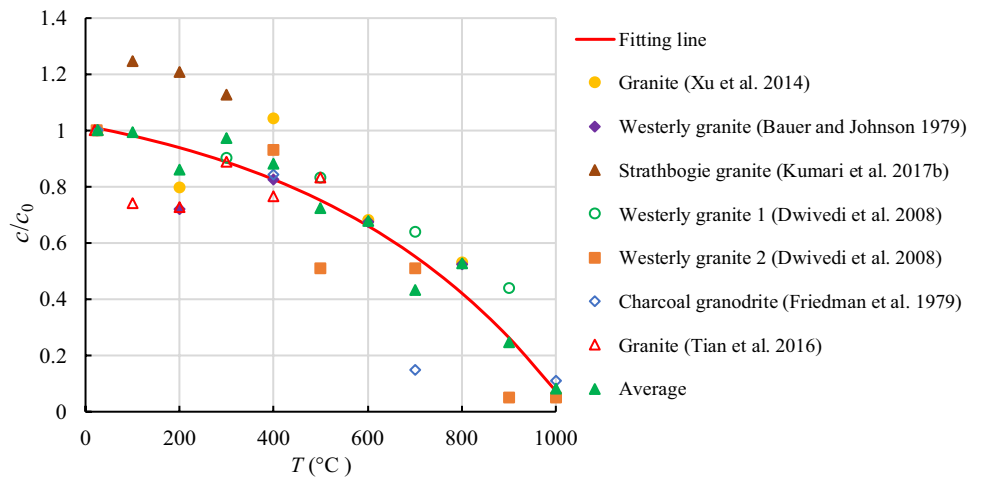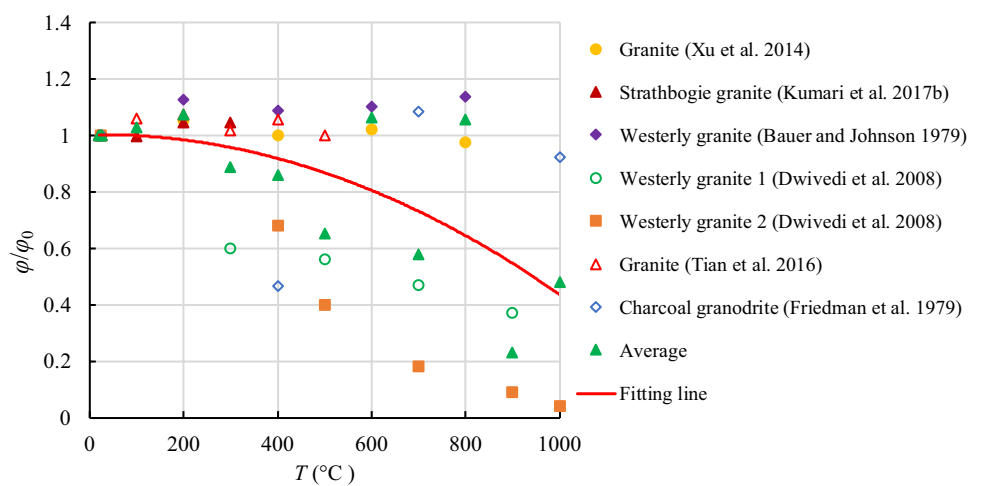**Fig. 5** Normalized cohesion of granites vs. temperature

Fig. 6 Normalized friction angle of granites vs. temperature

$$f_{c/c_0} = 0.1699\,(6.9845 - e^{0.001876T}),\ 0\,°C < T \leq 1000\,°C \tag{7}$$

$$f_{\varphi/\varphi_0} = -6 \times 10^{-7}T^2 + 3 \times 10^{-5}T + 1.0034,\ 0\,°C < T \leq 1000\,°C. \tag{8}$$

2.2 Temperature-Dependent Thermal Properties

2.2.1 Thermal Expansion

The coefficients of linear thermal expansion α_t and volumetric thermal expansion β_t are:

$$\alpha_t = \frac{1}{L}\frac{\Delta L}{\Delta T} \tag{9}$$

$$\beta_t = \frac{\partial \varepsilon_v}{\partial T}, \tag{10}$$

where L = length of the sample, ΔL = change in length of the sample, ΔT = change in temperature from the reference temperature, and ε_v = volumetric strain. In general, volumetric thermal expansion coefficient is three times the linear

coefficient, i.e. $\beta_t = 3\alpha_t$ (Ramana and Sarma 1980; Huotari and Kukkonen 2004).

Thermal expansion coefficients, which are proportional to the slope of thermal expansion curves [see Eqs. (9) and (10)], will increase sharply before the phase transition of quartz at $T_{\alpha-\beta} = 573\,°C$ and then reduce strongly within a short time (Van der Molen 1981; Hartlieb et al. 2015). This can be explained as follows: the quartz transition is combined with a large irreversible increase in volume and therefore substantial thermal microcracking takes place. The microcracking in turn changes the inner structure of the material by creating new or enlarged voids, which reduces the thermal expansion (Cooper and Simmons 1977; Polyakova 2014).

Measurements of thermal expansion coefficient for granites are quite rare beyond $T_{\alpha-\beta}$. Figure 7 shows normalized thermal expansion coefficients of granite and quartz at atmospheric pressure. Heuze (1983) illustrated the temperature dependency of the thermal expansion coefficient for different granites by a non-linear correlation and showed that at 573 °C the thermal expansion coefficient is about three times the value at room temperature (see Fig. 7). The thermal expansion of quartz and granite follows the same trend (Van

der Molen 1981; Hartlieb et al. 2015). In this case, the empirical correlation (see Fig. 7) from Chayé d'Albissin and Sirieys (1989) seems more reliable. There is a lack of data after 625 °C, but as a first approximation it is assumed that the coefficient is more or less constant beyond this temperature.

However, according to Hartlieb et al. (2015), granite can experience another further jump in thermal expansion between 800 and 900 °C. They explained this behaviour by a future phase transition of quartz to hexagonal tridymite at about 800 °C. But they also emphasised that the tridymite transition does only occur for quartz crystals with certain impurities and furthermore, differential thermal analysis (DTA) do not indicate a phase change. Up to now the knowledge in this direction is quite limited and does not allow to draw final conclusions.

Based on the correlation of Chayé d'Albissin and Sirieys (1989), the trend curve for the normalized coefficient of thermal expansion (Eq. 11) is shown in Fig. 7. The behaviour for $T > 800$ °C is not prescribed but can be added according to individual measurement results:

$$f_{\alpha_t/\alpha_{t0}} = \begin{cases} (0.8383 - 0.00142T)^{(-1/1.7085)}, & 0\ ^{\circ}\mathrm{C} \leq T \leq 573\ ^{\circ}\mathrm{C} \\ (-5.4160 + 0.0095T)^{(-1/1.5719)}, & 573\ ^{\circ}\mathrm{C} < T \leq 625\ ^{\circ}\mathrm{C} \\ f_{T=625}, & 625 < T \leq 800\ ^{\circ}\mathrm{C}. \end{cases}$$

(11)

2.2.2 Specific Heat

Figure 8 indicates that the increase of specific heat experience a discontinuity close to the α–β transition (Lindroth and Krawza 1971). The normalized trend curve is given by Eq. (12):

$$f_{C_v/C_{v0}} = \begin{cases} 0.957 + 6.59 \times 10^{-4}T, & 0\ ^{\circ}\mathrm{C} \leq T \leq 575\ ^{\circ}\mathrm{C} \\ 1.173 + 1.238 \times 10^{-4}T, & 573\ ^{\circ}\mathrm{C} \leq T \leq 1000\ ^{\circ}\mathrm{C}. \end{cases}$$
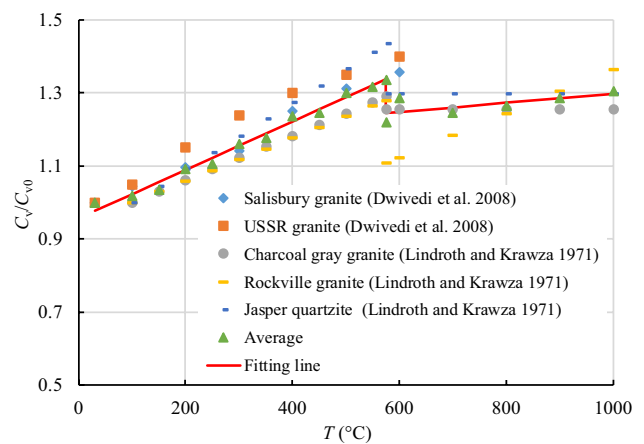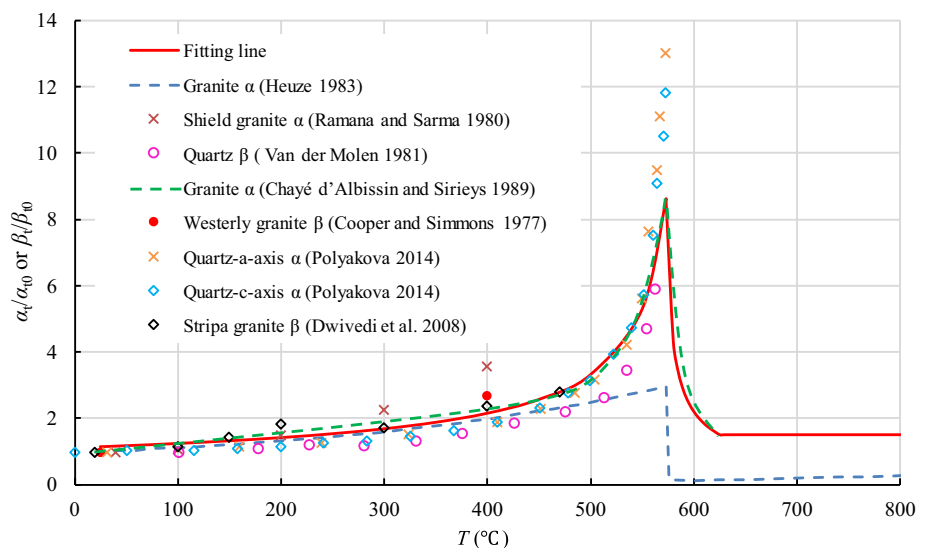
(12)

Fig. 8 Normalized specific heat of granites vs. temperature

2.2.3 Thermal Conductivity

An empirical law (Heuze 1983) for thermal conductivity k has been obtained from the test results of seven granites. From Fig. 9, we can see that the empirical law proposed by Heuze is also suitable for higher temperatures. Based on the data collection (e.g. Romine et al. 2012; Wen et al. 2015; Žák et al. 2006), a more reliable law is given by Eq. (13):

$$\begin{aligned} f_{k/k_0} = {}&-5.8126 + 6.8485 \times 0.9995^{T} \\ &+ 0.002172T, \quad 0\ ^{\circ}\mathrm{C} \leq T \leq 1200\ ^{\circ}\mathrm{C}. \end{aligned}$$

(13)

3 Numerical Modelling

3.1 Methodology

In this study, the continuum-based finite difference code FLAC^{3D} (Itasca Inc 2018) is used. The thermal option

Fig. 7 Normalized thermal expansion coefficient of granites vs. temperature: α and β refer to linear and volumetric values, respectively
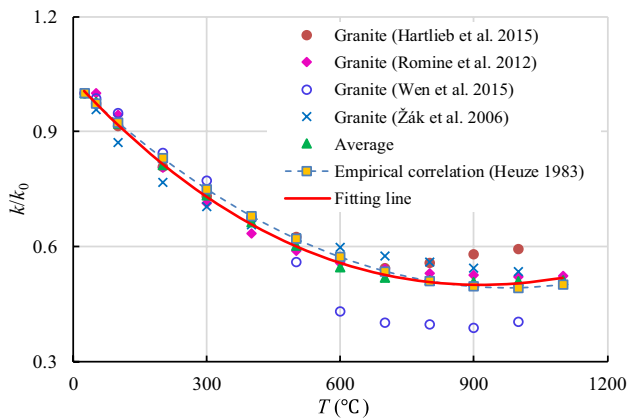
Fig. 9 Normalized thermal conductivity of granites vs. temperature

of FLAC^{3D} incorporates conduction models for thermal analysis. The mechanical models combined with isotropic conduction model allow the simulation of thermal-induced strains and stresses (thermo-mechanical coupling).

The basic expression based on the energy balance has the following form:

$$-q_{i,i} + q_v = \rho C_v \frac{\partial T}{\partial t}, \tag{14}$$

where q_i (W/m^2) is the heat flux vector, q_v (W/m^3) is the volumetric heat-source intensity, C_v (J/kg °C) is the specific heat at constant volume, and ρ (kg/m^3) is the mass density. The thermal conduction in the model is governed by Fourier's law, which equals to the product of thermal conductivity k (W/m °C) and the temperature gradient, $-\nabla T$ (°C/m). The heat transfer law has the form:

$$q_i = -k\nabla T. \tag{15}$$

The solution of thermal stress problems requires reformulation of the incremental stress–strain relations, which is accomplished by subtracting the portion due to temperature change from the total strain increment. Thermal stress and strain changes are given by the following expressions:

$$\Delta \sigma_{ij} = 3\delta_{ij} K \alpha_t \Delta T \tag{16}$$

$$\Delta \varepsilon_{ij} = \delta_{ij} \alpha_t \Delta T, \tag{17}$$

where α_t (1/ °C) is the coefficient of thermal expansion, ΔT is the temperature increment, K is the bulk modulus (Pa) and δ_{ij} is the Kronecker delta.

Previous thermo-mechanical models are homogeneous, which means the physical and thermo-mechanical properties of each element in the model have the same value. This might be an efficient way for large-scale applications, but for considerations at smaller scale (e.g., at the grain size level), the heterogeneity of physical and thermo-mechanical properties may become important. To reflect such an

inhomogeneity, the Weibull statistical distribution (Weibull 1951; Liu et al. 2004; Tan 2013) is applied for the thermo-mechanical parameters. If the basic property of the sample is P_0, the specific property of the numerical element i is P_i, and the corresponding Weibull random variable is x_i, then we obtain the randomly distributed property $P_i = P_0 \times x_i$.

Besides the classical Mohr–Coulomb model with tension cutoff (Itasca 2018), the strain-softening model is also used. The advantage of this law is that cohesion, friction, dilation and tensile strength can soften or harden after the onset of plastic yield according to a certain function. The softening table relating tension limit to plastic tensile strain and tables relating shear parameters (i.e., cohesion, friction angle, and dilation angle) to plastic shear strains are the same as in Sect. 5, where these parameters are back calculated from lab test results.

3.2 Model Description

3.2.1 Geometry and Boundary Conditions

A cylindrical granite specimen that was 50 mm in diameter and 100 mm in length was modelled as shown in Fig. 10a. Because of the extreme long run times of the models, only one quarter of the cylinder was used under the assumption of symmetry conditions. This holds for the homogeneous model, but is—in a strict sense—not correct for the inhomogeneous models. However, test calculations have shown that the deviation in terms of stress–strain behaviour, temperature evolution and damage pattern between the full cylindrical inhomogeneous model and the corresponding one-quarter model are extremely small. Based on this finding, all further simulations were performed with one-quarter models.

Displacements at the two perpendicular symmetry planes and the bottom were fixed in normal direction (Fig. 10b). The outer boundary temperature was fixed to the desired value.

3.2.2 Numerical Model Setup

Four approaches (Table 1) were applied in this section. In Weibull models, the shape parameter m characterizes the brittleness (high values for m enhance the brittleness and vice versa). Tan (2013) tested different shape parameters ($m = 5$ to $m = 40$) to simulate heterogeneous granite samples and found that it is extremely difficult to determine an accurate shape parameter. In our simulations, we set the shape parameter $m = 10$ and the scale parameter $x_0 = 1.05$.

Table 2 shows the initial thermo-mechanical granite properties at room temperature (25 °C). Figure 11 shows the tensile strength for homogeneous and heterogeneous models as an example.
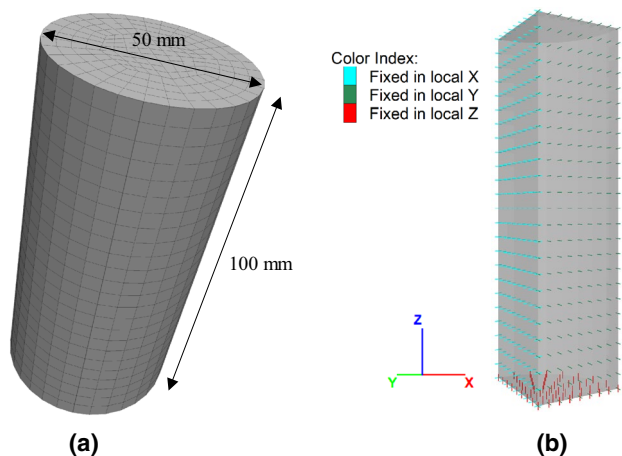
Fig. 10 Schematic diagram of the granite model

Table 1 Model approaches

Model	Constitutive law	Property distribution
1	Mohr–Coulomb	Homogeneous
2	Mohr–Coulomb	Weibull distribution
3	Strain softening	Homogenous
4	Strain softening	Weibull distribution

Homogeneous and heterogeneous models were built with fixed temperatures at the outer boundary (see Fig. 12). These models are based on the Mohr–Coulomb constitutive law. They are heated for 5 s with boundary temperature of 100 °C, 150 °C, 200 °C, and 300 °C, respectively. The failure states of the heterogeneous and homogeneous models are quite similar in terms of damage propagation. High boundary temperatures (e.g., 200 °C and 300 °C) can destroy the sample in a very short time (see Fig. 12c, d), but thermal cracking cannot be induced if the boundary temperature is too low such as 100 °C (see Fig. 12a). At 150 °C, thermal-induced damage increases gradually with measurable speed (see Fig. 12b). Therefore, we used 150 °C as fixed boundary temperature for the models documented in Sect. 3.

3.3 Influence of Property Distributions

3.3.1 Temperature Distribution

Figure 13a, b show temperature distributions of homogeneous and heterogeneous models, respectively. These two models are heated for 50 s with 150 °C at outer boundary. Homogeneous and heterogeneous models show slightly different temperature distribution patterns. Figure 13c shows that the biggest temperature difference between these two models is 0.86 °C. Equations (14) and (15) indicate that the heterogeneous properties (e.g., thermal

Table 2 Model parameters

Parameters	Initial values
Coefficient of linear thermal expansion, α_t (1/ °C)	8×10^{-6}
Specific heat, C_v (J/kg °C)	820
Thermal conductivity, k (W/m °C)	2.6
Young's modulus, E (GPa)	37.35
Poisson's ratio, ν	0.127
Tensile strength, σ_t (MPa)	13
Cohesion, c (MPa)	23
Friction angle, φ (°)	50
Dilation angle, ψ (°)	10
Density, ρ (kg/m^3)	2645

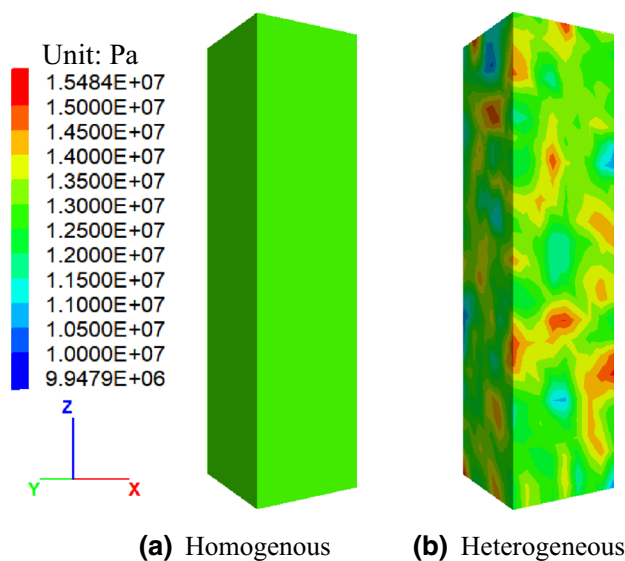**(a)** Homogenous   **(b)** Heterogeneous

Fig. 11 Distribution of tensile strength [Pa] of homogeneous and heterogeneous models

conductivity and specific heat) can influence the heat conduction, and consequently lead to changes in temperature gradient.

3.3.2 Thermal Stress and Deformation

Figure 14 shows differential stress distributions of models 1 and 2 according to Table 2 heated for 50 s with fixed boundary temperature of 150 °C. Figure 14a, b present the contours of the differential stresses in the XZ plane of the homogeneous model (i.e., model 1) and the heterogeneous model (i.e., model 2). The local stress fluctuations are the most obvious feature in the heterogeneous model. Figure 14b and d show the differential stresses at the surface of the two models, where biggest differential stresses are located at mid-height region in both models.

Fig. 12 Failure states of the homogeneous and heterogeneous Mohr–Coulomb models heated for 5 s with different temperatures at outer boundary
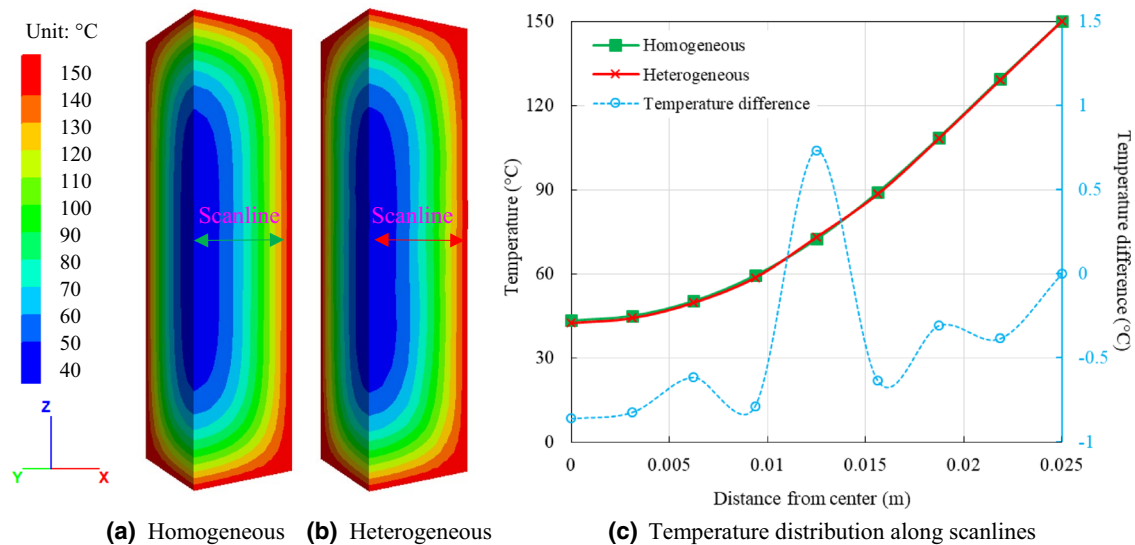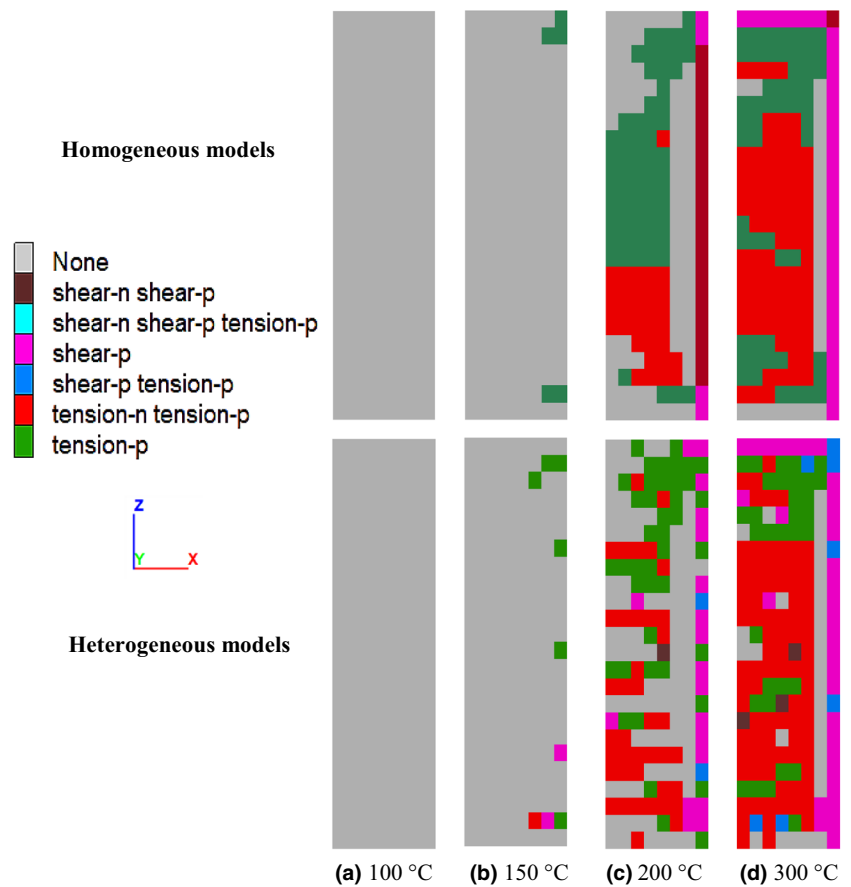

Homogeneous models

- None
- shear-n shear-p
- shear-n shear-p tension-p
- shear-p
- shear-p tension-p
- tension-n tension-p
- tension-p

Heterogeneous models

(a) 100 °C   **(b)** 150 °C   **(c)** 200 °C   **(d)** 300 °C

(a) Homogeneous   **(b)** Heterogeneous   **(c)** Temperature distribution along scanlines

Fig. 13 Temperature distributions (°C) of different models heated for 50 s with 150 °C at outer boundary

The general trend in respect to stress and strain (see Fig. 15) is the same for both models, but the heterogeneous model showed some fluctuations caused by the initial inhomogeneous thermo-mechanical parameter distributions.

3.3.3 Thermal-Induced Damage

Figure 16 shows that only tensile failure occurred in the homogeneous model, while inside the heterogeneous model in addition to some extent also shear failure can be observed.

Fig. 14 Differential stress ($\sigma1–\sigma3$) [Pa] distributions in plane XZ and at the surface of model 1 and 2 heated for 50 s with 150 °C at outer boundary
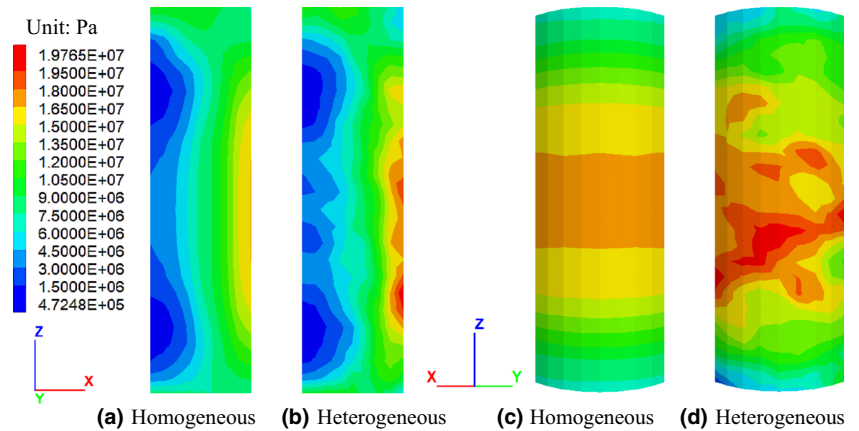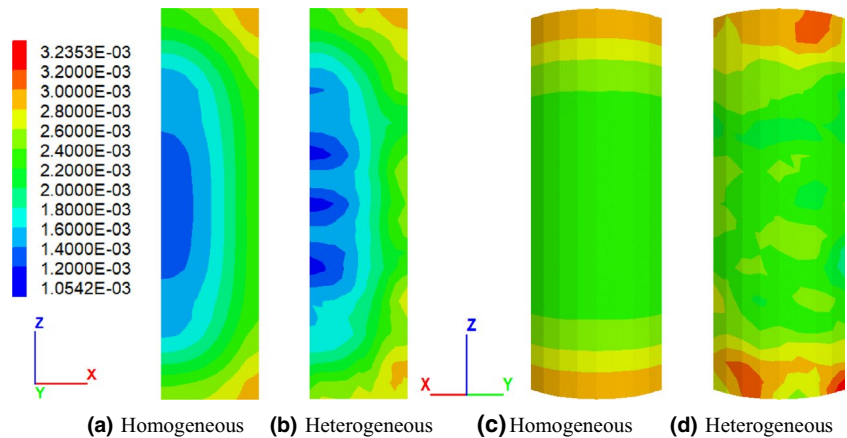

(a) Homogeneous **(b)** Heterogeneous **(c)** Homogeneous **(d)** Heterogeneous

Fig. 15 Volumetric strain in plane XZ and at the surface for model 1 and 2 heated for 50 s with 150 °C at outer boundary

(a) Homogeneous **(b)** Heterogeneous **(c)** Homogeneous **(d)** Heterogeneous

Another difference is that the outer surface of the homogenous model is undamaged except for the top and bottom. Lab tests and numerical simulations have shown that thermal-induced cracks are usually isolated and spread over the whole sample (Zhao 2016; Yang et al. 2017). In general, the failure pattern of the heterogeneous model is more realistic. It reproduces the general trend superimposed by some local fluctuations.

3.4 Influence of Constitutive Laws

Figure 17 shows the plasticity states models using the Mohr–Coulomb and the strain-softening model with heterogeneous property distributions (i.e., Model 2 and Model 4). The failure pattern of the strain-softening model (Fig. 17b) is similar to that of the Mohr–Coulomb model, but tends to produce more isolated cracks compared with the more connected failure zones shown in Fig. 17a. Obviously, the strain-softening model results in a more realistic failure pattern. Also, compared with the Mohr–Coulomb model, in general the strain-softening model can reflect the strength reduction and the post-failure behaviour of the sample in a more realistic way (Itasca 2018).
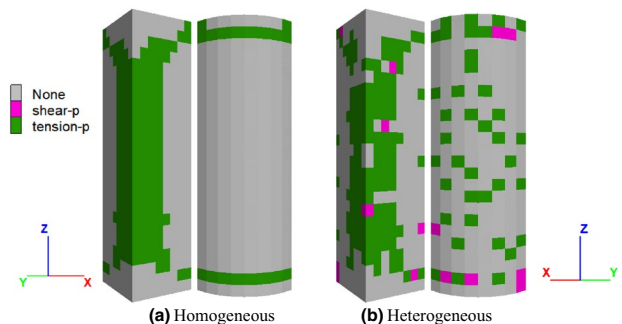

(a) Homogeneous **(b)** Heterogeneous

Fig. 16 Failure states for model 1 and 2 heated for 50 s with 150 °C at outer boundary

4 Sensitivity Analysis of Thermo-Mechanical Properties

There are eight important temperature-dependent parameters of granite. A sensitivity analysis was conducted to find out to what extend the different input parameters influence the simulation results.
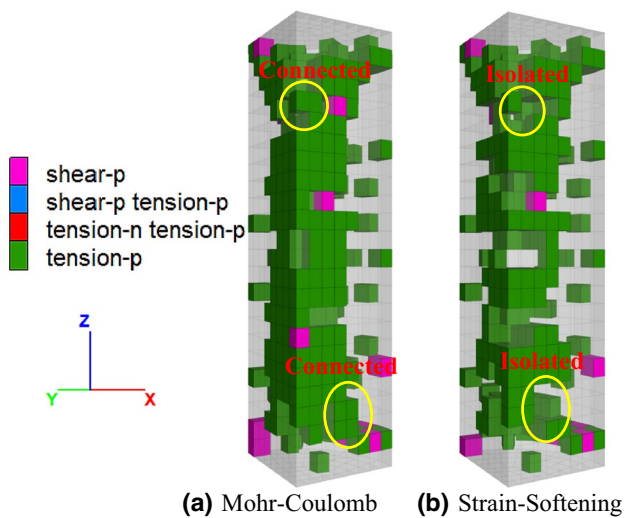
(a) Mohr-Coulomb   **(b)** Strain-Softening

Fig. 17 Plasticity states of model 2 and 4 heated for 50 s with 150 °C at outer boundary

The standard fire time–temperature curve given in ISO 834 is used for fire resistance tests. The temperature development is described by the following equation:

$$T = T_0 + 345\log(8t + 1), \tag{18}$$

where T_0 is room temperature in °C, T is the fire temperature in °C, and t is time in minutes.

According to Eq. (18), the average heating rate is 35 °C/min to reach 800 °C starting from 25 °C. Two boundary conditions were considered: (i) fixed boundary temperature of 800 °C for 50 s and (ii) constant heating rate of 35 °C/min at the outer boundary until 800 °C have been reached.

4.1 Model Description

The geometrical model for sensitivity analysis is the same as shown in Fig. 10. Table 3 shows the parameters used in the model. All the models use the same set of softening tables mentioned in Sect. 5. The simulations assume

Table 3 Parameters for sensitivity study

Parameters	Temperature-dependent values
Coefficient of linear thermal expansion, α_t (1/ °C)	$\alpha_t(T) = 8 \times 10^{-6} \times f_{\alpha t/\alpha t0}$
Specific heat, C_v (J/kg °C)	$C_v(T) = 820 \times f_{Cv/Cv0}$
Thermal conductivity, k (W/m °C)	$k(T) = 2.6 \times f_{k/k0}$
Young's modulus, E (GPa)	$E(T) = 37.35 \times f_{E/E0}$
Poisson's ratio ν	$\nu(T) = 0.127 \times f_{\nu/\nu0}$
Tensile strength, σ_t (MPa)	$\sigma_t(T) = 13 \times f_{\sigma t/\sigma t0}$
Cohesive strength, c (MPa)	$c(T) = 20 \times f_{ct/c0}$
Friction angle, φ (°)	$\varphi(T) = 50 \times f_{\varphi t/\varphi0}$
Dilation angle, ψ (°)	10 (constant)
Density, ρ (kg/m³)	2645 (constant)

temperature-dependent variations of mechanical and thermal properties via the corresponding trend curves given in Sect. 2. For each boundary condition, a reference model was built where all the eight parameters are temperature independent. Except for the parameters to be investigated, all other input parameters are the same as in the reference model. The results are shown in form of difference values related to the reference model.

4.2 Thermo-Mechanical Behaviour with Temperature-Dependent Parameters

4.2.1 Temperature Distribution

Figure 18a shows the temperature variations along the scanline (see Fig. 13) for a model heated for 50 s with a constant boundary temperature of 800 °C. All the values were processed by subtracting the data of the reference model. We can see that only two parameters, specific heat and thermal conductivity, have effects on temperature distribution. Thermal conductivity plays a more important role than specific heat, causing the largest 91.9 °C temperature decrease. Figure 18b shows the simulation results for the model heated up to 800 °C with a heating rate of 35 °C/min. Specific heat shows a more obvious influence under these conditions, but thermal conductivity still contributes most to the temperature variations. In the central area of the sample, the temperature-dependent properties lead to a temperature difference up to 91.2 °C.

4.2.2 Thermal-Induced Stresses

Figure 19 shows variations of principal stresses induced by temperature-dependent parameters under constant boundary temperature of 800 °C after 50 s of heating. Both maximum and minimum principal stresses are strongly influenced by thermal expansion coefficient, thermal conductivity, Young's modulus, and tensile strength. All temperature-dependent parameters lead to a significant localized increase in stresses which subsequently results in more isolated failures across the sample.

Compared with the model of constant boundary temperature, thermal stresses in proximity to the outer boundary are sensitive to property variations considering a heating rate of 35 °C/min (Fig. 20). This is because the heating rate results in a continuous temperature increase near the boundary, thus causing variations in thermal stresses according to Eq. (16). Another noticeable phenomenon is that cohesive strength becomes more important in the model with a constant heating rate.

In both scenarios, the influence of friction angle, specific heat, and Poisson's ratio on stress changes is relatively small. The impact of friction angle especially can be ignored
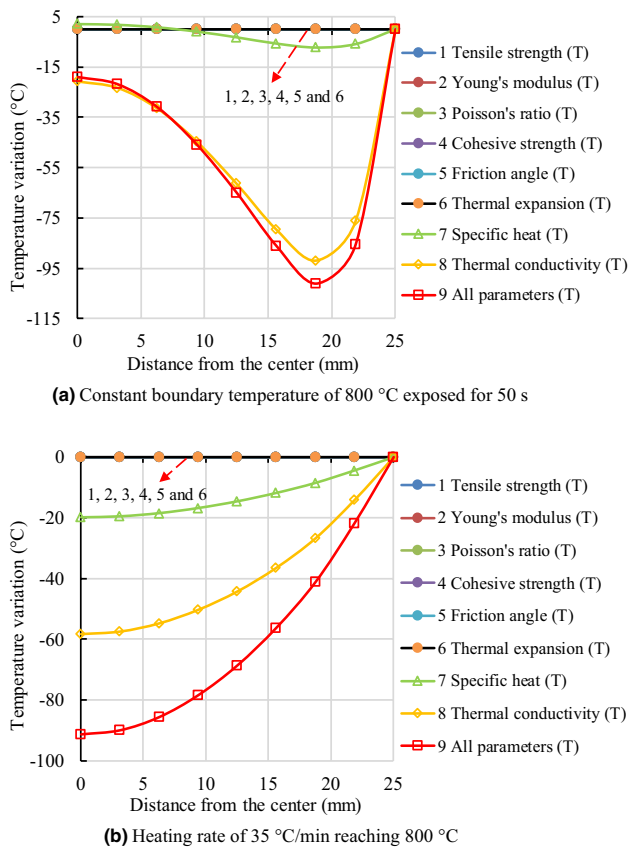
(a) Constant boundary temperature of 800 °C exposed for 50 s

(b) Heating rate of 35 °C/min reaching 800 °C

Fig. 18 Temperature variations along the scanline for models with different heating conditions at outer boundary considering different parameters

(a) Maximum principal stress σ_1

(b) Minimum principal stress σ_3

Fig. 19 Stress variations along scanline for model with a constant boundary temperature of 800 °C after 50 s of heating considering different parameters

compared to other parameters. Nevertheless, thermal expansion coefficient, thermal conductivity, tensile strength, and Young's modulus always have a significant influence on thermal stress evolution.

4.2.3 Thermal-Induced Deformations

Displacements are greatly influenced by thermal expansion coefficient, Young's modulus, and thermal conductivity under constant boundary temperature scenario (Fig. 21a). Obviously, thermal expansion coefficient contributes most, while thermal conductivity leads to a slightly opposite behaviour. The reason is that thermal expansion coefficient increases strongly with increasing temperature (see Fig. 7), while thermal conductivity has an opposite trend (see Fig. 9) which results in a decrease of temperature increment (see Fig. 18). Consequently, the displacement is reduced according to Eq. (17).
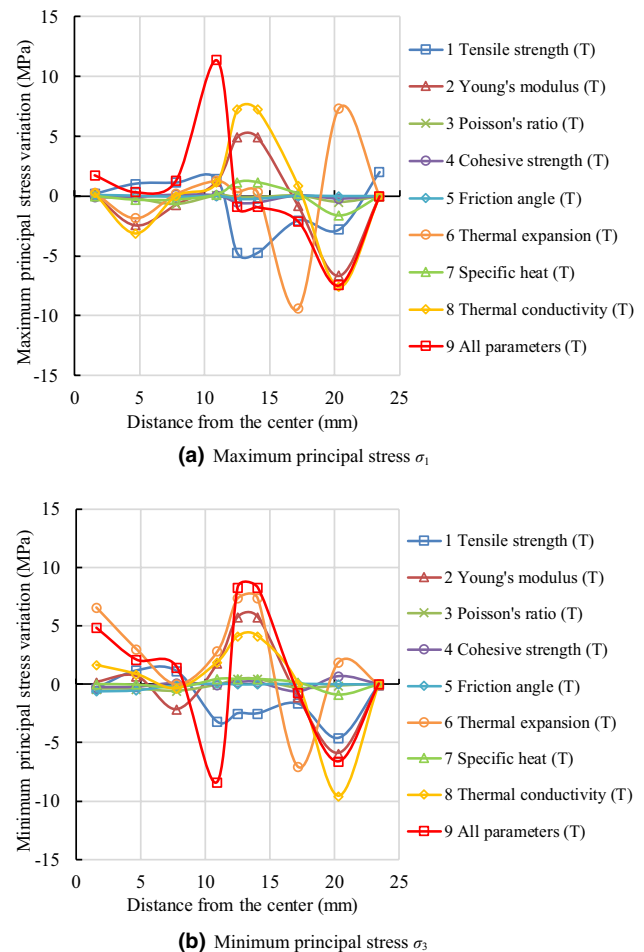
The variations of properties under constant boundary temperature also induce the expansion and contraction of granite (see Fig. 21b). Figure 19b shows, that when all parameters are temperature dependent, there is a big local increase in compressive stress (for example, at a distance of 10.9 mm). This is why the volumetric strain increment of the grain becomes negative (i.e., contraction). As expected, largest grain expansion takes place at the boundary.

In the second scenario with a heating rate of 35 °C/min, the linear thermal expansion coefficient dominates the displacements again (see Fig. 22a). Other temperature-dependent parameters have only insignificant influence. Figure 22b shows the volumetric strain variations for a heating rate of 35 °C/min. Again, thermal expansion coefficient determines the dilatation of the granite.
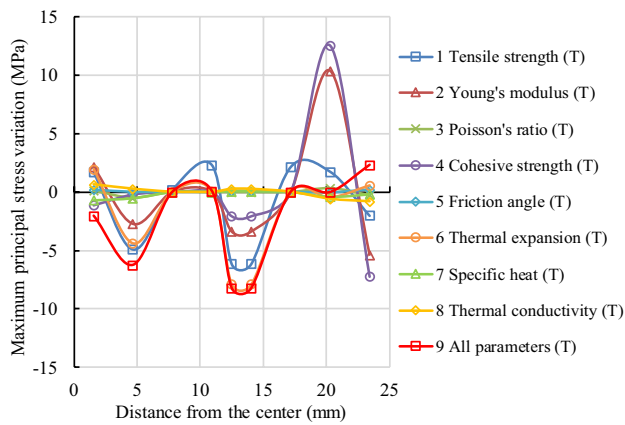
(a) Maximum principal stress σ_1
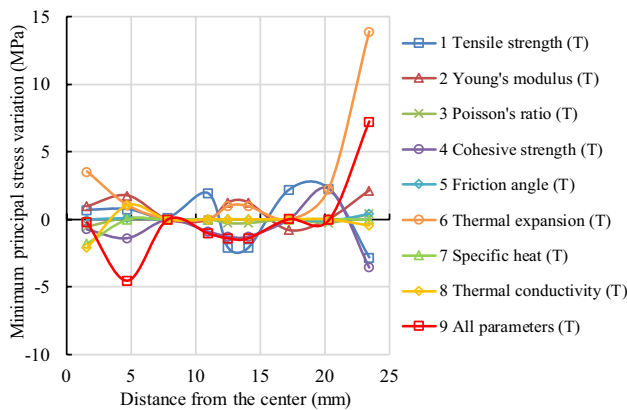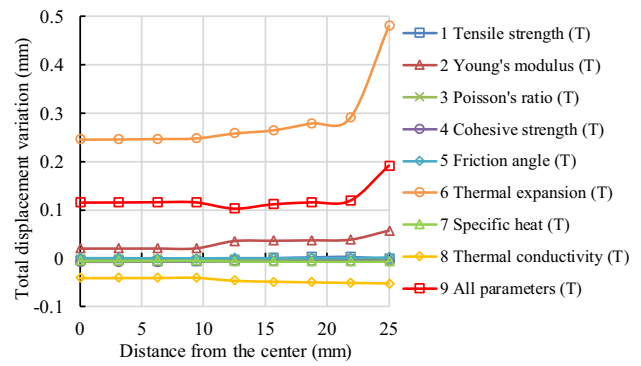

(b) Minimum principal stress σ_3

Fig. 20 Stress variations along scanline for model with a heating rate of 35 °C/min reaching 800 °C considering different parameters
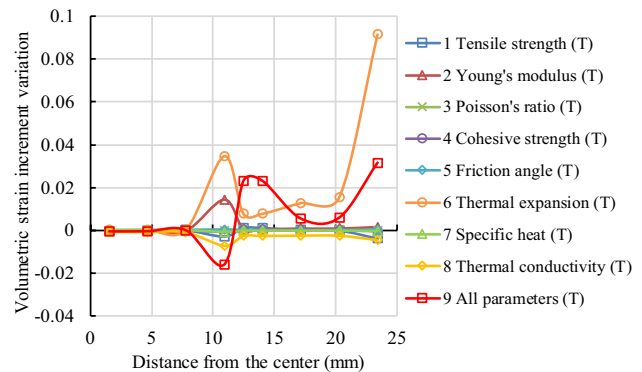

(a) Total displacement variations

(b) Volumetric strain increments

Fig. 21 Deformations along scanline for model with a constant boundary temperature of 800 °C after 50 s of heating considering different parameters

5 Validation of the Proposed Model

5.1 Model Description

A quarter of a three-dimensional model with 6500 elements was set up with a radius of 25 mm and a height of 100 mm. All parameters are assigned according to a Weibull distribution with the shape parameter $m = 15$ and the scale parameter $x_0 = 1.036$. The geometrical boundary is fixed as shown in Fig. 10. The model was heated at a rate of 5 °C/min and then kept at target temperatures for 30 min to achieve nearly homogeneous final temperature distribution. The simulation is based on the assumptions that in lab testing: (1) thermal cracking and strength reduction only occurs during the heating process, and that there is no more property change once the temperature of the sample becomes uniform; (2) the influence of thermal gradient during the naturally cooling process up to room temperature can be neglected.

The axial stress–strain curves for uniaxial loaded granite specimens after thermal treatments show that the behaviour changes dramatically beyond 600 °C (Yang et al. 2017): up to the peak stress the material is much softer and beyond the peak stress the brittleness is lost. The loss of brittleness is associated with the density of thermal cracks in the specimen (Yang et al. 2017). When temperature is beyond 600 °C and increased to 700 °C, larger cracks can be induced. Optical microscopic observations of granite specimens at $T = 800$ °C show that more and more thermal-induced cracks have formed. Many thermal-induced microcracks in the 800 °C specimens have also encouraged crack interaction and coalescence, which leads to further increase crack density and aperture compared with the specimen at $T = 600$ °C. This means that crack density and crack apertures increase with increasing temperature, especially after 600 °C. As a result, the fractured specimens become softer, and the granites are not that brittle any more. Zuo et al. (2017) suggested that 250 °C could be considered as a threshold for the brittle ductile transition for some granites. The noticeable nonlinearity and yielding phase before peak load indicate the loss of brittle characteristic of granite.
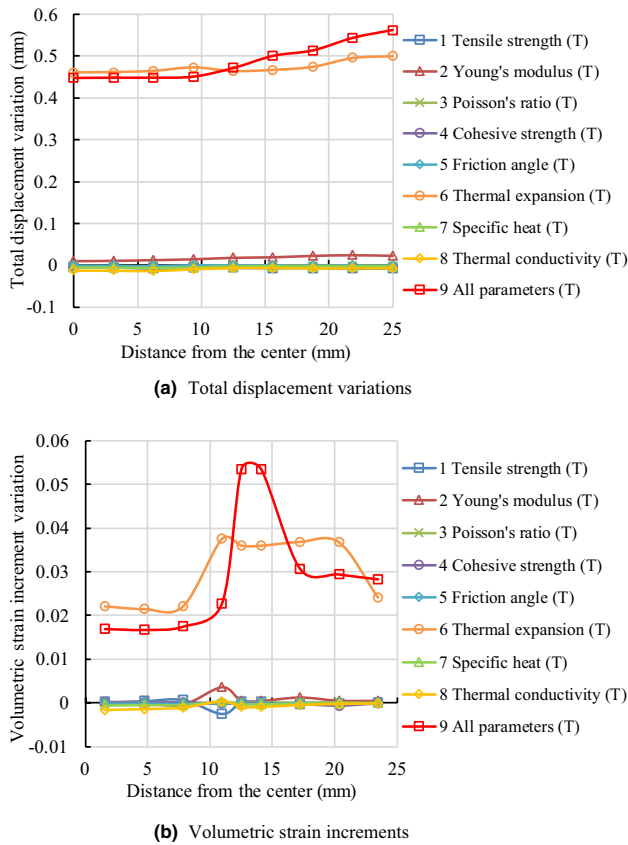
(a) Total displacement variations

(b) Volumetric strain increments

Fig. 22 Deformations along scanline for model with a heating rate of 35 °C/min reaching 800 °C considering different parameters

Table 4 Back-analysed parameters used for numerical modelling

Sample/°C	ν_s (Yang et al. 2017)	ρ/kg/m^3 (Yang et al. 2017)	E_c/GPa	E_{input}/GPa	c/MPa
25	0.127	2643	26.96	29.5	15.88
200	0.098	2633	26.84	31	18.10
300	0.109	2632	30.83	36	20.20
400	0.095	2628	22.155	29	16.40
500	0.041	2608	16.21	21	15.00
600	0.038	2565	11.12	14	10.85
700	0.244	2449	2.73	3.56	5.80
800	0.367	2358	1.27	1.70	3.70

(see Fig. 20), and is therefore back analysed carefully for different temperatures (Fig. 23c). Although these back-calculated softening parameters fit this lab test very well (nearly perfect), future analyses of more lab tests are necessary to obtain general softening laws. All the other parameters are the same as in Table 3. The sketch of the final numerical model is illustrated in Fig. 24.

5.2 Thermal Damage Characteristics

Optical microscopic observations (Yang et al. 2017) showed that 200 °C has not caused any visible thermal-induced microcracks. Many boundary and transgranular cracks became visible when sample was heated up to 400 °C, but most grains still remain intact. At $T = 600$ °C, microcracks have propagated across most grains with an obvious increase in crack quantity and width.

Figure 25 shows plasticity states in numerical models for different temperatures. Failed elements can be interpreted as thermal-induced microcracks. Just as the optical observations show (see Yang et al. 2017), nearly no failures occur at $T = 200$ °C (see Fig. 25a). At $T = 400$ °C (Fig. 25b), more zones fail in tension, but still many zones remain undamaged. However, the majority of zones experience tensile failure at 600 °C (Fig. 25c), indicating a large number of tensile microcracks. The evolution of plasticity states in the numerical model can well reflect the microcrack generation in granite at elevated temperatures.

It should be noticed that at 600 °C, microcracks cannot be captured by X-ray CT technique with a minimum resolution of 30 μm (Yang et al. 2017). Only a few macrocracks wider than 30 μm can be observed at 700 °C, while the number of macrocracks shows an abrupt rise at 800 °C. The scanning results also illustrate the inhomogeneous behaviour of thermally induced cracks, which are isolated from each other and widespread over the whole sample (Yang et al. 2017).
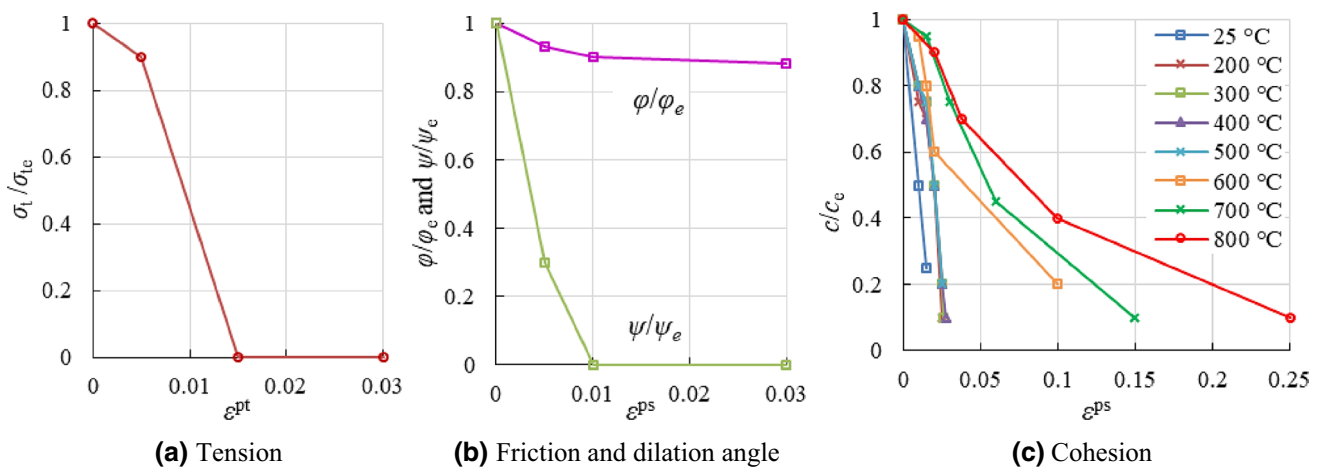
To characterize the stiffness of the sample, a threshold modulus E_c obtained from dividing peak axial stress σ_c by the peak axial strain ε_{1c} is defined (Yang et al. 2017). The input Young's modulus E_{input}, which governs the elastic behaviour before yielding should be back analysed based on E_c. Table 4 shows the input parameters used in the model. They are implemented as temperature-dependent properties in form of fitting equations for certain temperature ranges (e.g., 25–200 °C, 200–300 °C, etc.). Friction angle φ is set to 50° and is temperature independent. Cohesive strength c and softening parameters (i.e., tables for cohesion, dilation, friction and tension) are back calculated from lab test results. Figure 23 shows the softening parameters used in this model. If tensile crack width (corresponds to plastic tension strain) is large enough, the tensile strength of the element is approaching zero (Fig. 23a). Considering that friction angle has negligible influence on the thermomechanical behaviour, as the sensitivity analysis revealed, and assuming that dilation angle will approach zero after shear failure, they follow softening laws without temperature dependency (Fig. 23b). It has been discovered that cohesive strength has obvious impact on thermal stress distribution

Fig. 23 Variation of softening parameters with plastic strain. ε^{pt} is the plastic tension strain, ε^{ps} is the plastic shear strain, and subscript 'e' means the property at plastic strain $\varepsilon^{p} = 0$
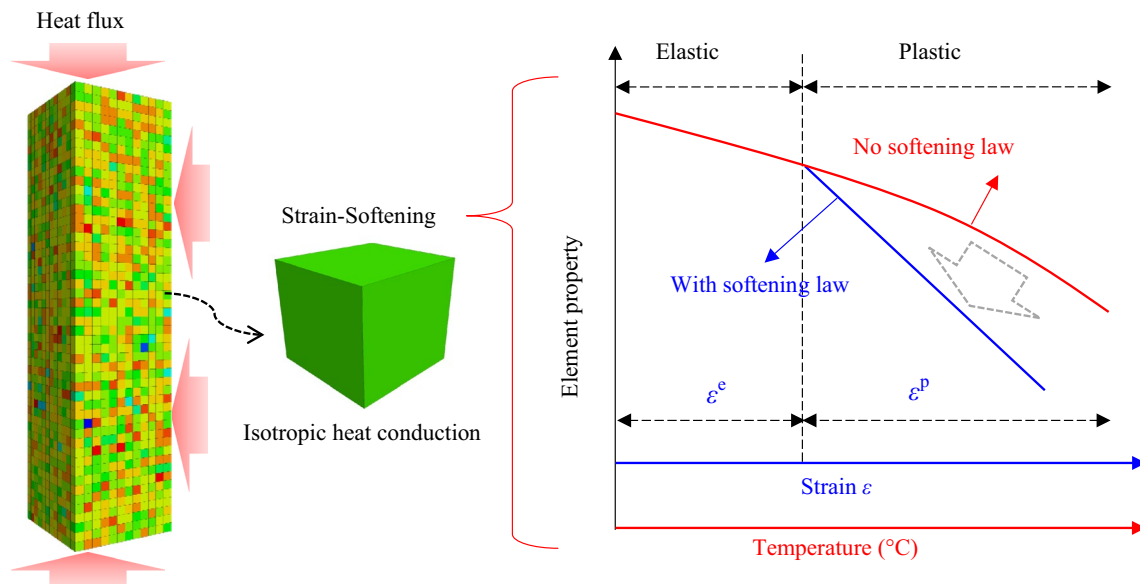

Fig. 24 Sketch of the established model for thermo-mechanical simulation. ε^{e} is the elastic strain, ε^{p} is the plastic strain

However, the cracks in FLAC^{3D} cannot be observed directly. An indirect method can be used for investigating thermally induced cracks with various widths. In a simplified manner, we assume that the strain of thermally induced cracks of granite equals the tensile plastic strain in the numerical model. The length of model elements is between 1.1×10^{-3} and 2.6×10^{-3} m. The smallest width of the macrocracks is 30 μm. Then we can deduce that the minimum plastic strain for macrocrack generation is about 1.15×10^{-2} to 2.73×10^{-2}. Figure 26 shows the plastic tensile strain at 700 °C for horizontal cross-sections at different height. The

calculated plastic strains at 700 °C are mainly in order of 10^{-3}, only a few elements have plastic tensile strain larger than 10^{-2}. When heated to 800 °C (Fig. 27), the macrocrack density is significantly increased as also shown in the lab tests (see Yang et al. 2017).

Figure 28 shows the plastic tensile strains in vertical cross-sections. From the strain distribution, we can infer that macrocracks with width greater than 30 μm can hardly be observed at temperatures up to about 600 °C (Fig. 28a), but a large number of isolated macrocracks are formed at temperatures between 700 and 800 °C (Fig. 28b, c). This is in
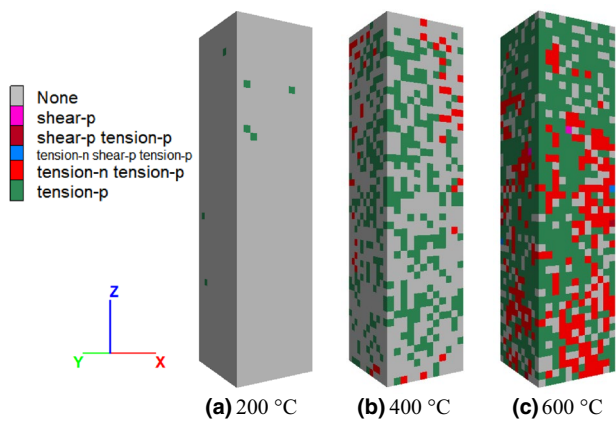
Fig. 25 Plasticity states of the sample at different temperatures

a remarkable consistency with lab observations (Yang et al. 2017), although strain contours are only an indirect way to investigate real cracks. Figure 29a shows elements with plastic tensile strain larger than 1.15×10^{-2} (corresponds to crack width larger than 30 µm in lab test) at 800 °C. Figure 29b documents that thermal cracks are also quite distinct and covering the whole sample similar to the lab observations (Yang et al. 2017).

5.3 Mechanical Test After Heat Treatment

After heat treatment, the thermo-mechanical coupling is deactivated and the simulation is continued by pure mechanical uniaxial compression test at room temperature. This procedure is consistent with the lab test procedure. Figure 30 shows the vertical stress–strain relations for samples heated up to different temperatures before. The brittle characteristic of granite is obvious for temperatures up to about 300 °C, but above this temperature ductility becomes more and more predominant. These curves reproduce quite well the lab test results obtained by Yang et al. (2017).

Table 5 documents the peak values of axial stress σ_{cs} and the corresponding strain ε_{cs} obtained from the simulations. The relative error of stress and strain (δ_σ and δ_ε) between lab test and numerical simulation are also documented. As Fig. 31 shows, peak axial stress and strain have a great consistency with the lab test results (Yang et al. 2017). This verifies again the accuracy and physical plausibility of the developed numerical model used in this study.

6 Conclusions

1. Although lab data about the thermo-mechanical behaviour of granite at high temperatures up to about 1000 °C are quite rare, it becomes obvious that most material

Fig. 26 Plastic tensile strain at 700 °C for horizontal cutting planes at different height

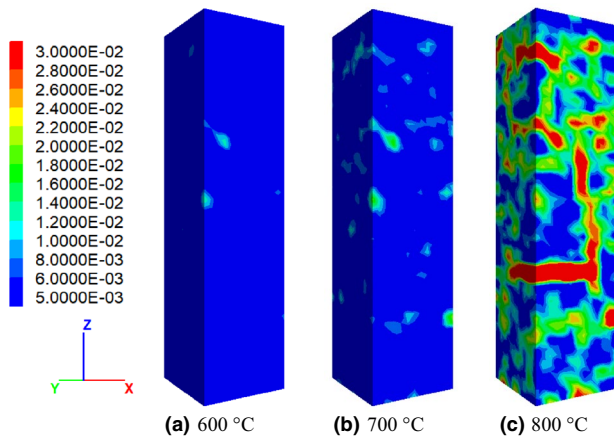**Fig. 27** Plastic tensile strain at 800 °C for horizontal cutting planes at different height

Fig. 28 Plastic tensile strain observed at vertical cutting planes at different temperatures
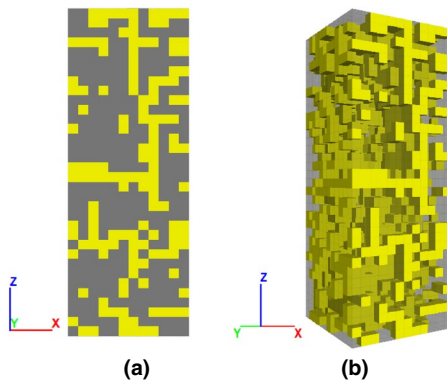

Fig. 29 Granite at 800 °C: **a** Simulated macrocracks along vertical cross-section. **b** Simulated 3D macrocrack pattern
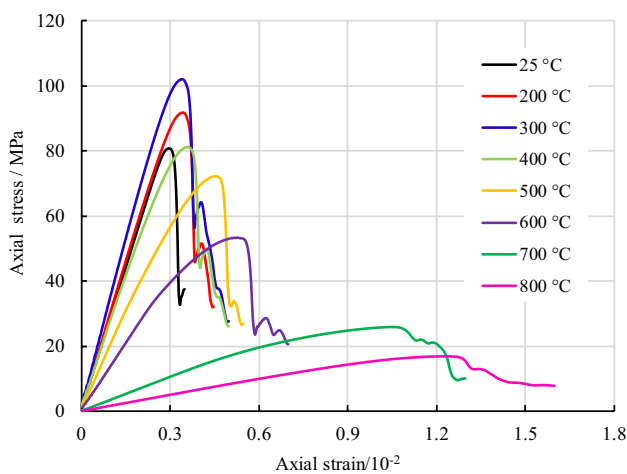

Fig. 30 Simulated stress–strain relations for uniaxial compression tests on samples exposed to different temperatures before

Table 5 Simulation results of peak axial stress and strain

Specimen/°C	σ_{cs}/MPa	δ_σ/%	ε_{cs}/10^{-2}	δ_ε/%
25	80.73	0.84	0.297	0
200	91.74	1.72	0.343	2.08
300	102.02	− 0.02	0.342	3.32
400	81.19	− 0.66	0.361	− 2.17
500	72.23	− 0.07	0.455	2.02
600	53.33	− 4.07	0.527	5.4
700	25.89	− 6.53	1.057	4.04
800	16.84	9.71	1.214	0.33

parameters (except for friction angle) experience a significant change with increasing temperature due to thermal-induced cracking. Besides a more continuous change of the parameters up to nearly 600 °C, the α–β transition of quartz leads to an abrupt jump in some parameters (especially Poisson's ratio, thermal expansion coefficient and specific heat). Although microscopic thermal damage starts already at low temperatures, only beyond 600 °C strong macroscopic thermal cracking is observed.

2. Based on an extensive analysis of existing data, general relations between temperature and several thermo-mechanical parameters were established. Several versions of the well-known Mohr–Coulomb constitutive model with tension cutoff and strain softening were extended by the established thermo-mechanical parameter relations to investigate the potential of realistic simulation of thermal-induced damage.

3. Simulation results indicate, that a modelling strategy using a Mohr–Coulomb model with strain softening and tension cutoff in combination with stochastic parameter distribution and temperature-dependent adjustment of parameters (tensile strength, Young's modulus, cohesive strength, thermal conductivity, Poisson's ratio, thermal expansion coefficient, specific heat) allows to simulate thermal-induced damage in a realistic manner. The comparison of damage and fracture patterns as well as stress–strain relations between lab data and numerical simulations based on the new proposed procedure show a remarkable agreement, which can be considered as the first validation of the proposed modelling strategy.
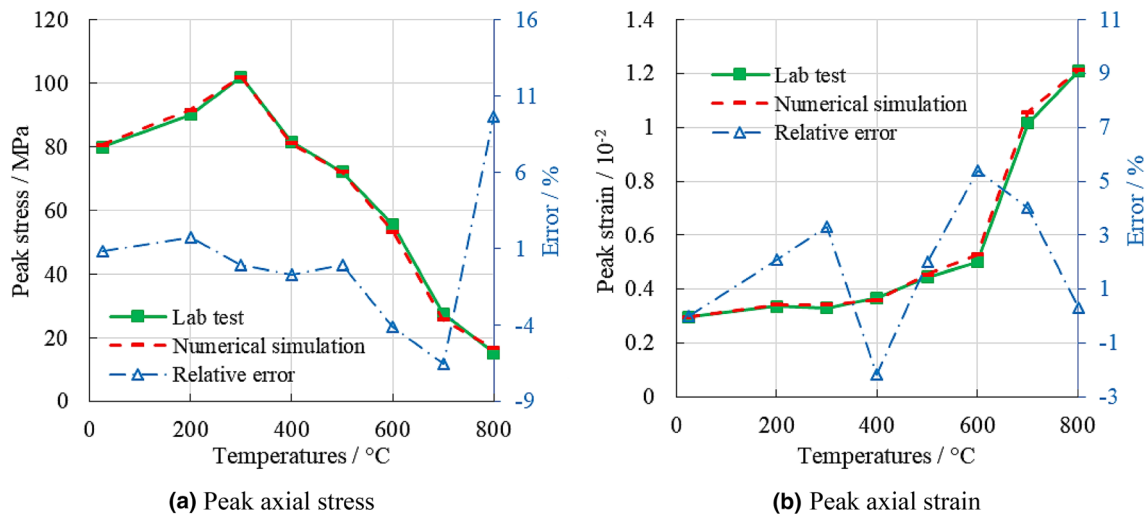
(a) Peak axial stress

(b) Peak axial strain

Fig. 31 Comparison of simulation and lab test results

References

Bauer SJ, Johnson B (1979) Effects of slow uniform heating on the physical properties of the Westerly and Charcoal granites. In: 20th US symposium on rock mechanics (USRMS). American Rock Mechanics Association

Brotóns V, Tomás R, Ivorra S et al (2013) Temperature influence on the physical and mechanical properties of a porous rock: San Julian's calcarenite. Eng Geol 167:117–127

Chayé d'Albissin M, Sirieys P (1989) Thermal deformability of rocks: relation to rock structure. In: Maury and Fourmaintraux (eds) Rock at great depth. Balkema, Rotterdam, pp 363–370

Chen YL, Wang SR, Ni J et al (2017) An experimental study of the mechanical properties of granite after high temperature exposure based on mineral characteristics. Eng Geol 220:234–242

Cooper HW, Simmons G (1977) The effect of cracks on the thermal expansion of rocks. Earth Planet Sci Lett 36(3):404–412

David C, Menéndez B, Darot M et al (1999) Influence of stress-induced and thermal cracking on physical properties and microstructure of La Peyratte granite. Int J Rock Mech Min Sci 36:433–448

David EC, Brantut N, Schubnel A, Zimmerman RW (2012) Sliding crack model for nonlinearity and hysteresis in the uniaxial stress-strain curve of rock. Int J Rock Mech Min Sci 52:9–17

Dwivedi RD, Goel RK, Prasad VVR et al (2008) Thermo-mechanical properties of Indian and other granites. Int J Rock Mech Min Sci 45(3):303–315

Freire-Lista DM, Fort R, Varas-Muriel MJ (2016) Thermal stress-induced microcracking in building granite. Eng Geol 206:83–93. https://doi.org/10.1016/j.enggeo.2016.03.005

Friedman M, Handin J, Higgs NG et al (1979) Strength and ductility of four dry igneous rocks at low pressures and temperatures to partial melting. In: 20th US symposium on rock mechanics (USRMS). American Rock Mechanics Association, pp 35–50

Gautam PK, Verma AK, Maheshwar S et al (2016) Thermomechanical analysis of different types of sandstone at elevated temperature. Rock Mech Rock Eng 49(5):1985–1993

Glover PWJ, Baud P, Darot M et al (1995) α/β Phase transition in quartz monitored using acoustic emissions. Geophys J Int 120:775–782

Griffiths L, Heap MJ, Baud P, Schmittbuhl J (2017) Quantification of microcrack characteristics and implications for stiffness and strength of granite. Int J Rock Mech Min Sci 100:138–150

Hartlieb P, Toifl M, Kuchar F et al (2015) Thermo-physical properties of selected hard rocks and their relation to microwave-assisted comminution. Miner Eng. https://doi.org/10.1016/j.mineng.2015.11.008

Heap MJ, Lavallée Y, Laumann A et al (2013) The influence of thermal-stressing (up to 1000 °C) on the physical, mechanical, and chemical properties of siliceous-aggregate, high-strength concrete. Constr Build Mater 42:248–265

Heuze FE (1981) Geotechnical modeling of high-level nuclear waste disposal by rock melting (No. UCRL-53183). Lawrence Livermore National Lab., CA (USA)

Heuze FE (1983) High-temperature mechanical, physical and thermal properties of granitic rocks—a review. Int J Rock Mech Min Sci Geomech Abstr 20(1):3–10

Hoek E, Brown ET (1997) Practical estimates of rock mass strength. Int J Rock Mech Min Sci 34(8):1165–1186

Huotari T, Kukkonen I (2004) Thermal expansion properties of rocks: literature survey and estimation of thermal expansion coefficient for Olkiluoto mica gneiss. Posiva Oy, Olkiluoto, Working Report 4

Itasca Consulting Group, Inc (2018) FLAC3D fast lagrangian analysis of continua in 3 dimensions—FLAC3D help. Minneapolis, Minnesota

Jiao YY, Zhang XL, Zhang HQ et al (2015) A coupled thermo-mechanical discontinuum model for simulating rock cracking induced by temperature stresses. Comput Geotech 67:142–149

Kumari WGP, Ranjith PG, Perera MSA et al (2017a) Temperature-dependent mechanical behaviour of Australian Strathbogie granite with different cooling treatments. Eng Geol 229:31–44

Kumari WGP, Ranjith PG, Perera MSA et al (2017b) Mechanical behaviour of Australian Strathbogie granite under in situ stress and temperature conditions: an application to geothermal energy extraction. Geothermics 65:44–59

Lindroth DP, Krawza WG (1971) Heat content and specific heat of six rock types at temperatures to 1000 °C. Rep. Invest.-US, Bureau of Mines (United States), p 7503

Liu HY, Roquete M, Kou SQ et al (2004) Characterization of rock heterogeneity and numerical verification. Eng Geol 72(1–2):89–119

Nasseri MHB, Schubnel A, Young RP (2007) Coupled evolutions of fracture toughness and elastic wave velocities at high crack density in thermally treated Westerly granite. Int J Rock Mech Min Sci 44:601–616

Nasseri MHB, Tatone BSA, Grasselli G, Young RP (2009) Fracture toughness and fracture roughness interrelationship in thermally treated westerly granite. Pure Appl Geophys 166:801–822

Panji M, Koohsari H, Adampira M et al (2016) Stability analysis of shallow tunnels subjected to eccentric loads by a boundary element method. J Rock Mech Geotech Eng 8:480–488

Polyakova IG (2014) The main silica phases and some of their properties. Glass Sel Prop Cryst. https://doi.org/10.1515/9783110298581.197

Ramana YV, Sarma LP (1980) Thermal expansion of a few Indian granitic rocks. Phys Earth Planet Inter 22(1):36–41

Romine WL, Whittington AG, Nabelek PI et al (2012) Thermal diffusivity of rhyolitic glasses and melts: effects of temperature, crystals and dissolved water. Bull Volcanol 74(10):2273–2287

Saiang C, Miskovsky K (2012) Effect of heat on the mechanical properties of selected rock types–a laboratory study. In: 12th ISRM Congress, Beijing, China, pp 815–820

Shao S, Ranjith PG, Wasantha PLP et al (2015) Experimental and numerical studies on the mechanical behaviour of Australian Strathbogie granite at high temperatures: an application to geothermal energy. Geothermics 54:96–108

Tan X (2013) Hydro-mechanical coupled behavior of brittle rocks. Dissertation, Technische Universität Bergakademie Freiberg

Tian H, Mei G, Zheng MY (2016) Rock properties after high temperatures (in Chinese). China University of Geosciences Press, Wuhan

Török A, Török Á (2015) The effect of temperature on the strength of two different granites. Cent Eur Geol 58(4):356–369

Van der Molen I (1981) The shift of the α–β transition temperature of quartz associated with the thermal expansion of granite at high pressure. Tectonophysics 73(4):323–342

Vásárhelyi B (2009) A possible method for estimating the Poisson's rate values of the rock masses. Acta Geod Geophys Hungarica 44:313–322

Weibull W (1951) A statistical distribution function of wide applicability. J Appl Mech 18(3):293–297

Wen H, Lu JH, Xiao Y et al (2015) Temperature dependence of thermal conductivity, diffusion and specific heat capacity for coal and rocks from coalfield. Thermochim Acta 619:41–47

Xu XL, Gao F, Zhang ZZ (2014) Research on triaxial compression test of granite after high temperatures. Rock Soil Mech 35(11):3177–3183

Xu T, Zhou GL, Heap MJ et al (2017) The influence of temperature on time-dependent deformation and failure in granite: a mesoscale modeling Approach. Rock Mech Rock Eng 50(9):2345–2364

Yang SQ, Ranjith PG, Jing HW et al (2017) An experimental investigation on thermal damage and failure mechanical behavior of granite after exposure to different high temperature treatments. Geothermics 65:180–197

Yong C, Wang CY (1980) Thermally induced acoustic emission in Westerly granite. Geophys Res Lett 7(12):1089–1092

Žák J, Vyhnálek B, Kabele P (2006) Is there a relationship between magmatic fabrics and brittle fractures in plutons?: a view based on structural analysis, anisotropy of magnetic susceptibility and thermo-mechanical modelling of the Tanvald pluton (Bohemian Massif). Phys Earth Planet Inter 157(3–4):286–310

Zhao Z (2016) Thermal influence on mechanical properties of granite: a microcracking perspective. Rock Mech Rock Eng 49(3):747–762

Zuo JP, Wang JT, Sun YJ et al (2017) Effects of thermal treatment on fracture characteristics of granite from Beishan, a possible high-level radioactive waste disposal site in China. Eng Fract Mech 182:425–437